

# Rupture process of 2011 Mw7.1 Van, Eastern Turkey earthquake from joint inversion of strong-motion, high-rate GPS, teleseismic, and GPS data

A. Ozgun Konca

Received: 16 November 2014 / Accepted: 2 July 2015 / Published online: 2 August 2015  
© Springer Science+Business Media Dordrecht 2015

**Abstract** We analyzed the rupture process of the 2011  $M_w$ 7.1 Van, Eastern Turkey earthquake using teleseismic, strong-motion, 1-Hz GPS waveforms and static GPS displacement measurements. We performed data sensitivity analyses using four different rupture scenarios. Overall, when geodetic and seismic datasets are modeled jointly, slip distribution is well-constrained and rupture velocity can be obtained. The 2011 Van earthquake is a case where none of the available datasets are sufficient to constrain the slip distribution and the rupture kinematics on their own. This study confirms that rather than fitting one dataset perfectly, using multiple datasets jointly leads to a better-constrained slip distribution. The kinematic model obtained from the joint inversion of all the available data shows a 45-km-long bilateral rupture with two sub-events; one larger slip patch propagating up-dip and toward west of the hypocenter and a smaller second slip patch toward the east. The highest slip is to the west of the hypocenter with a peak value of 4.5 m. The slip is confined to the depths of 7.5 to 20 km and the shallower part of the fault remains unbroken. The average rupture velocity is around 3 km/s, close the Rayleigh wave velocity. The

rupture is faster with shorter rise times for the larger sub-event toward the west, while the rise times are longer for the smaller sub-event to the east. This difference in seismic behavior might be related to the segmentation of the fault.

**Keywords** 2011 Van earthquake · Earthquake source · Earthquake physics · Finite-fault modeling

## 1 Introduction

On October 21, 2011,  $M_w$ 7.1 Van Earthquake occurred in Eastern Anatolia, causing significant damage around the epicenter and taking more than 600 lives. Eastern Anatolia is a plateau that is under compression due to the convergence of the Arabian Plate and the Eurasian Plate (Dewey et al. 1986) at a rate of 2.3 cm/year (Reilinger et al. 2006). Bitlis Suture Zone marks the boundary between the Arabian Plate to the south and Anatolian Microplate to the north (Dewey et al. 1986) (Fig. 1). The tectonic character of Eastern Anatolia is predominantly determined by the compressive forces: E-W trending thrust faults and NE-SW trending left lateral and NW-SE trending strike-slip faults (Sengor and Yilmaz 1981). To the west of the Karliova Triple Junction, two strike-slip fault systems, the right lateral North Anatolian Fault Zone (Barka 1992) and the left lateral Eastern Anatolian Fault Zone (Arpat and Saroglu 1972), accommodate the collision by escape tectonics (Sengor et al. 1985) (Fig. 1). To the east of the Karliova Triple Junction, the deformation is more distributed and

---

**Electronic supplementary material** The online version of this article (doi:10.1007/s10950-015-9506-z) contains supplementary material, which is available to authorized users.

---

A. O. Konca (✉)  
Department of Geophysics, Bogazici University, Kandilli  
Observatory and Earthquake Research Institute,  
34684Cengelkoy, Istanbul, Turkey  
e-mail: ozgun.konca@boun.edu.tr

the motion is accommodated by conjugate strike-slip faults and a few thrust and normal faults (Orgulu et al. 2003). The total shortening across the 250-km Eastern Anatolia Plateau is about 10 mm/year based on long-term GPS measurements (Reilinger et al. 2006; Elliott et al. 2013).

The 2011 earthquake occurred on the east-west trending Van fault on the E-SE of the Karliova Triple Junction (Fig. 1). No surface rupture was observed in the preliminary field surveys (Emre et al. 2011). However, later studies showed that the earthquake did create small-scale deformation along a length of ~12 km with a strike of 255°, before entering Lake Van (Elliott et al. 2013). The existence of the Van fault had been documented earlier; however, its activity was relatively unknown before the 2011 earthquake. The General Directorate of Mineral Research and Exploration of Turkey (MTA) did not include this fault in its active fault map (Saroglu et al. 1992; Emre et al. 2011). A study of earthquake mechanisms in Eastern Anatolia (Orgulu et al. 2003) includes an  $M_w$ 5.3 earthquake (denoted in Fig. 1) to the west of the 2011 rupture with a similar mechanism showing that the Van fault was indeed active and that it extends into Lake Van (Fig. 1). There is no local study of the strain accumulation across the Van fault; however, using a profile from Reilinger et al. (2006), Elliott et al. (2013) inferred that the strain accumulation across the fault must be less than 5 mm/year.

In this study, we model the spatiotemporal history of the Van earthquake using teleseismic, near-source (including strong-motion and 1-Hz GPS data), as well as GPS static displacement data. So far, the slip distribution of the 2011 Van earthquake has been studied using teleseismic, InSAR, GPS, and strong-motion data separately but no finite-fault model using joint datasets have been released (Utkucu 2013; Elliott et al. 2013; Gallovic et al. 2013; Altiner et al. 2013; Evangelidis and Kao 2013). In addition, we successfully integrated the 1-Hz GPS waveforms as part of the analysis, which had not been studied to this date for this particular event. The goal of this study is to examine the contribution of each dataset and provide a detailed spatiotemporal model of the earthquake.

We start by thoroughly examining the contribution of each dataset by carrying out synthetic resolution tests for four different rupture scenarios. Then, we perform a grid search to constrain the average rupture velocity to be used as a reference rupture velocity. Using this reference rupture velocity, we perform variable rupture velocity

inversions using the datasets separately and together. We obtain a kinematic model for the 2011 Van earthquake using all the datasets. We compare the final slip distribution of this study with prior studies of the earthquake using single type of data and discuss the possible reasons for the significant variations in slip distributions among different groups. Finally, we discuss the slip distribution and kinematic properties of the earthquake.

## 2 Datasets

In order to study the source kinematics of the 2011 earthquake, we utilized static GPS displacements, teleseismic waveforms, near-source seismic data including two strong-motion, and one high-rate GPS station waveforms.

### 2.1 GPS displacement data

The static GPS displacements due to the  $M_w$ 7.1 Van earthquake were processed by Scientific and Technological Research Council of Turkey (TUBITAK) (Dr. Rahsan Cakmak, personal communication) using daily GPS solutions before and after the Van earthquake and were downloaded from the Super Sites website (<http://supersites.earthobservations.org/van.php>). Static displacements were measured for 20 GPS stations. Our initial modeling shows that five of these stations are either too far away to contribute to the model or their errors are too large and cannot be explained by slip on a fault. Therefore, we included only 15 of these stations in the analysis (Fig. 1).

### 2.2 Teleseismic data

Teleseismic data (30°–90° distance) were downloaded from IRIS website. The stations were selected to ensure good azimuthal coverage and low signal-to-noise ratio. 19 P and 10 SH waveforms were used in this study (Fig. 1, inset). The instrument response was removed, and the data was integrated to obtain the ground displacement. The data was band-pass filtered between 0.02 and 0.33 Hz.

### 2.3 Near-source seismic data

Two strong-motion stations and one high-rate GPS station waveforms were used for the inversion.

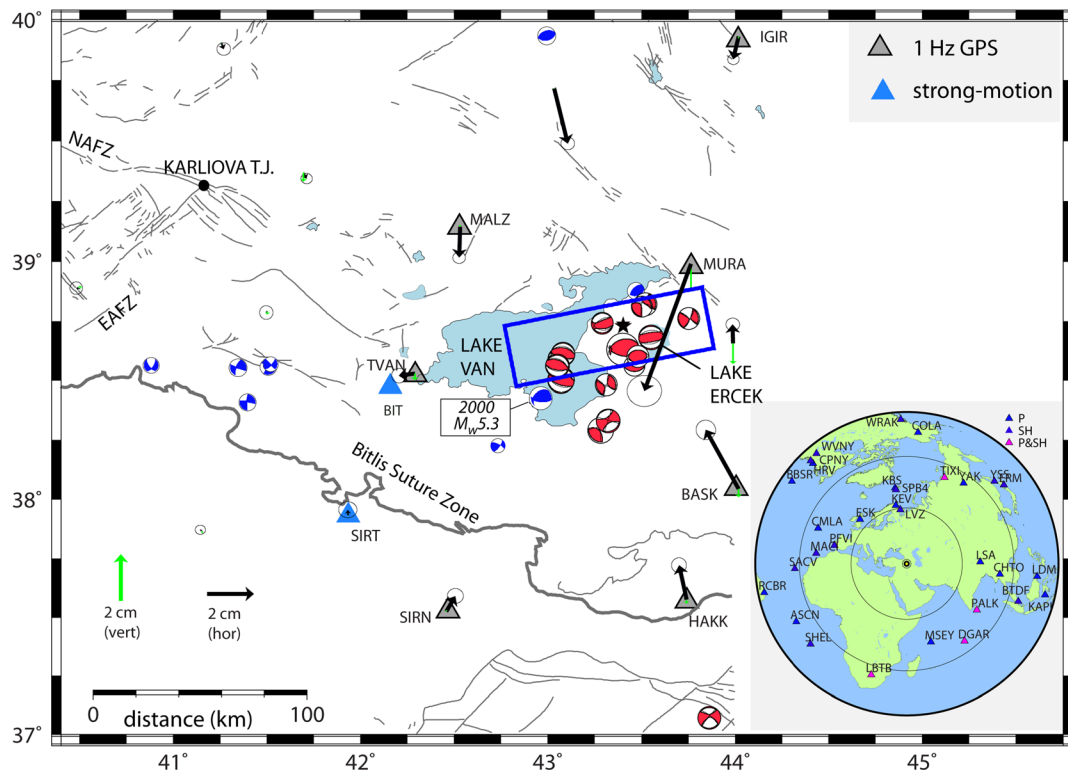


**Fig. 1** Datasets and the rupture area of the 2011 Van earthquake. The *black* and *green arrows* indicate horizontal and vertical GPS data, respectively. The *circles* on the horizontal data indicate  $1\sigma$  errors for the GPS offset measurements. 1-Hz GPS stations that are used as seismic data are shown by *gray triangles* and their names are indicated. The location of the strong-motion stations are indicated by *blue triangles*. The *red beach balls* show the moment tensor of the aftershocks from the Global CMT catalog

(Dziewonski et al. 1981; Ekstrom et al. 2012), while the *blue beach balls* are the CMT solutions of regional earthquakes recorded during the Eastern Turkey Seismic Experiment in 1999–2000 (Orgulu et al. 2003). The *inset* shows the map view of the teleseismic data that are used in this study. *NAFZ*: North Anatolian Fault Zone, *EAFZ*: East Anatolian Fault Zone, *Karlioiva T.J.*: Karlioiva Triple Junction

Near-source data include seismic data recorded at no more than 150 km distance from the hypocenter (Fig. 1).

### 2.4 Strong-motion data

The strong-motion data were provided by the General Directorate of Disaster Affairs of Turkey (AFAD). Two stations, BIT and SIRT, were selected based on the waveform quality (Fig. 1). The strong-motion data were integrated twice to obtain the displacement waveforms. The band-pass filter was applied between 0.02 and 0.33 Hz for velocity seismograms to avoid instability that might occur when integrating acceleration data to displacement.

We chose to use displacement waveforms in the inversion because the 1-Hz GPS record is a displacement record and the noise level of the velocity

waveforms can be too large. In addition, since the two strong-motion stations are 100 to 150 km from the rupture, we avoided using the velocity seismograms which are more sensitive to the details of the Green’s function.

### 2.5 High-rate GPS data

The utilization of high-rate GPS (H-R GPS) time series for seismic studies are becoming widespread since its first use for the 2002 Denali Earthquake (Larson et al. 2003). The H-R GPS has since been used for studying various earthquakes (e.g., Ji et al. 2004; Delouis et al. 2010; Yin et al. 2013). The comparison of H-R GPS with the co-located strong-motion stations show that the motion recorded by the H-R GPS stations are coherent with those from strong-motion stations, especially for the displacement records (Wang et al. 2007, 2013).

The GPS data from the Turkish Continuously Operating Reference Station network (TR-CORS) were made available by the Turkish General Directorate of Land Registry and Cadaster (GDLRC) and the General Command of Mapping (GCM) ([http://www.hgk.msb.gov.tr/van\\_depremi\\_metin.htm](http://www.hgk.msb.gov.tr/van_depremi_metin.htm)). The 1 and 30 s sampled time series were already used to estimate the co-seismic static displacement in a few studies (Fielding et al. 2013; Altiner et al. 2013; Elliott et al. 2013; Gallovic et al. 2013; Moro et al. 2014). However, the displacement time series of H-R GPS data (1 Hz) were not studied to this date. Only 1-h H-R data were made available to the science community by the GCM; therefore, we were unable to apply special filters, such as the modified sidereal filter, to remove the low frequency errors (Choi et al. 2004).

In this study, TRACK kinematic software package (Herring 1998; Yin et al. 2013) was used to process the H-R GPS data, using the final orbits from IGS with 10° satellite elevation mask angle. The HORS station, located ~200 km north of the earthquake area, is used as the reference point. The position of the HORS station is fixed to the International Terrestrial Reference Frame (ITRF) 2008.0, epoch 2011 coordinates. For all other sites, positions in a local coordinate system (north, east, and vertical) are estimated every second with a loose a priori constraint (100 m). We were able to obtain the displacement time series of six sites (MALZ, HAKK, IGIR, MURA, TVAN, SEMD, SIRN) out of 15 stations of TR-CORS (Fig. 1).

Due to higher noise level in the H-R GPS data, we refrained from using these waveforms directly in our inversion. In order to determine which stations to include, we first performed a joint kinematic model using the strong-motion and teleseismic waveforms along with the static GPS displacements. We then used this finite-fault model to forward predict the time-dependent displacements at the H-R GPS site locations. In order to measure the similarity of the model predictions with the observed waveforms, we calculated the variance reduction (VR) for each horizontal H-R GPS displacement waveform using

$$VR = 100 \times \left[ 1 - \frac{\sum_{i=1}^n (d^i - s^i)^2}{\sum_{i=1}^n (d^i)^2} \right] \tag{1}$$

where  $d^i$  and  $s^i$  are the data and synthetic waveforms for the  $i$ th station, respectively.

Figure 2 shows the H-R GPS waveforms and the predictions from the joint inversion of strong-motion, teleseismic, and GPS data. Using a threshold of 50 % VR for both of the horizontal components as a selection criterion and considering the data amplitude and proximity to the fault rupture, we decided to include only the MURA station, which is only 42 km from the hypocenter and has recorded observable static offsets (Fig. 2).

We did not filter the H-R GPS data for plotting purposes, since it recorded significant static offset. However, for the inversion, we applied the same wavelet transform to the data and the synthetic waveforms (see “Methods”), hence the frequency range used for

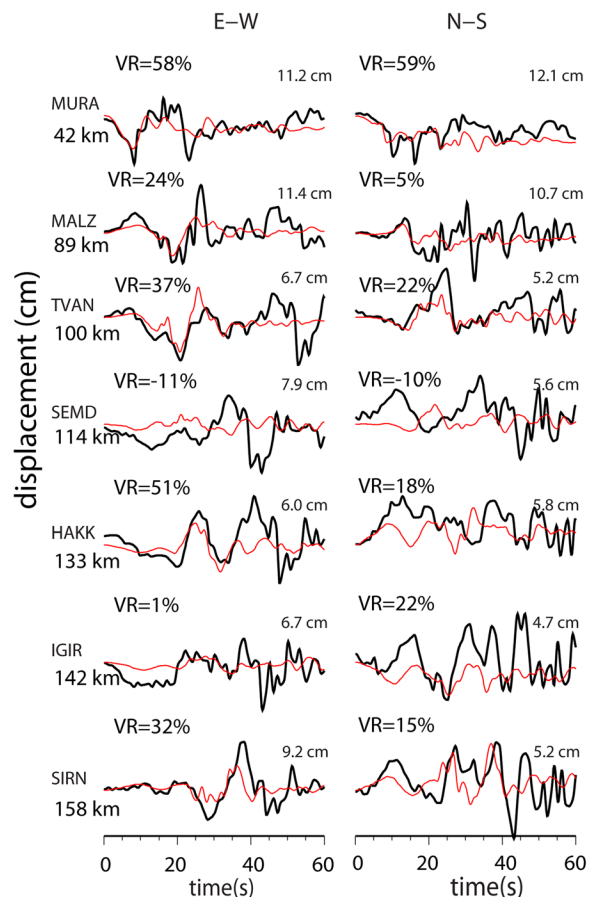


**Fig. 2** Horizontal components of the near-source high-rate GPS displacement waveforms (*black*) and the predicted synthetic waveforms from the joint teleseismic–static GPS model (*red*). The variance reduction (defined in Eq. 1) is shown on top of each waveform. The station names and the station distance to the hypocenter are displayed on the *left*. The peak displacement value of each waveform is shown on the *top right*

inversion is identical to the remaining seismic waveforms (0.02 to 0.33 Hz).

### 3 Methods

In order to obtain the kinematic solution for the 2011 Van earthquake, we used the method of Ji et al. (2002), which is capable of performing joint inversion of teleseismic, geodetic, and near-source data (Ji et al. 2003; Konca et al. 2007, 2008, 2013). This inversion code employs the simulated annealing method, which is a global error minimization algorithm that searches a predetermined bounded parameter space, starting from a random model and converges to the best-fitting model. The joint inversion requires fitting the near-source and teleseismic seismograms, static displacement data, and the regularization constraints simultaneously.

The misfit to the waveforms is calculated in the wavelet domain in order to utilize the sensitivity to various frequency bands. In this study, the wavelet frequencies are between 0.02 and 0.33 Hz for the seismic data. The misfit between the observed and predicted waveforms is quantified in the wavelet domain using the weighted sum of L1 and L2 norms (Ji et al. 2002):

$$e_{wf} = \sum_{j=j_{min}}^{j=j_c} W_j \cdot \left( \frac{1}{k_j} \sum_k |o_{j,k} - y_{j,k}| + \sqrt{\frac{1}{k_j} \sum (o_{j,k} - y_{j,k})^2} \right) \tag{2}$$

where  $o_{j,k}$  and  $y_{j,k}$  are the wavelet coefficients of the observed and synthetic seismograms for the station  $k$  and the wavelet index  $j$ , and  $w_j$  is the weight of each wavelet channel. In this study, we keep the same weight on each wavelet channel  $w_j$ .

The misfit between the observed and the predicted static displacements is quantified from the root mean square of the residuals:

$$e_{stat} = \frac{1}{n} \sum_{i=1}^{i=n} (\text{pred}^i - \text{obs}^i)^2 \tag{3}$$

where  $n$  is the number of geodetic observations,  $\text{obs}^i$  is the observed displacement at station  $i$ , and  $\text{pred}^i$  is the predicted displacement at station  $i$ .

We regularize the inverse problem by applying space and time smoothness. Space smoothing is accomplished by minimizing the Laplacian of the slip distribution (slip smoothness) and time smoothing is done by minimizing the deviation from a constant reference rupture velocity given a priori. The objective function is then written as'

$$O = e_{wf} + w_{stat}e_{stat} + w_s\Delta_s + w_T\Delta_T \tag{4}$$

where  $w_{stat}$  is the weight put on the misfit to the static displacement data,  $w_s$  is the weight put on the Laplacian of the slip distribution, and  $w_T$  is the weight put on the Laplacian of the rupture time (the differential time at which the rupture front reaches each node with respect to a reference constant rupture velocity given a priori). The weight on the rupture time smoothing is calibrated to be large enough to avoid non-causal slip.

In the joint inversion, each dataset (near-source seismic, teleseismic, and static GPS) is weighted equally. The horizontal components of the 1-Hz GPS data have half the weight of the strong-motion data due higher noise level. The vertical component of 1-Hz GPS data was not included in the inversion due to low signal-to-noise ratio.

The seismic data are aligned based on their hand-picked first arrival time. For the alignment of the H-R GPS station MURA, hand-picking is not possible since the first arrival is not observable due to high noise level. To overcome this problem, we first performed a forward prediction of the displacement from the joint inversion of the GPS, teleseismic, and the two available strong-motion stations. Then we predicted the arrival times by aligning the predicted waveforms with the 1-Hz GPS data (Fig. 2).

### 4 Fault geometry

To this date, various strike and dip values have been reported for the 2011 earthquake using both seismology and geodesy. USGS reported the strike and dip as  $255^\circ/50^\circ$  from teleseismic body waves and  $272^\circ/19^\circ$  from CMT solutions while global CMT reported the solution as  $248^\circ/36^\circ$  (<http://earthquake.usgs.gov/earthquakes/eqinthenews/2011/usb0006bqc/>).

In order to resolve this uncertainty of fault geometry, we performed a grid search for the best strike and dip angle by using teleseismic and GPS data. Considering

the significant distance of the stations and uncertainty of Green's functions, we determined which near-source seismic station to use only after fixing the fault geometry and performing a preliminary waveform prediction using a joint teleseismic and GPS model. Hence, the near-source seismic data were not included in the initial grid search for the fault geometry.

For the grid search, we built a finite-fault geometry for possible strike and dip angle combination between  $220^{\circ}$ – $270^{\circ}$  and  $35^{\circ}$ – $85^{\circ}$  with  $5^{\circ}$  spacing, respectively (Fig. S1). Our analysis shows that the teleseismic and GPS datasets are relatively insensitive to the changes in strike and dip and various combinations of strike and dip angles fit the data equally well. Since the GPS stations are not very close to the fault and they are sparse, they do not constrain the geometry very well. We conclude that the available GPS and teleseismic dataset is not sufficient to well-constrain the fault strike and dip angles.

The only dataset that covers the fault area extensively from close distance is the InSAR data. Therefore, we chose to use the strike and dip obtained from an inversion for the best-fitting geometry using the InSAR data (Fielding et al. 2013) yielding strike and dip angle values of  $259^{\circ}$  and dip  $42.5^{\circ}$ , respectively. Similar values have been reported by Elliott et al. (2013), using the same InSAR tracks. The field observations which were made close to the western end of the rupture also agree with the strike obtained from the InSAR data (Elliott et al. 2013).

In order to test the effects of the fault geometry on our final kinematic model, we performed joint inversions of all the data (teleseismic, static GPS, strong-motion, and H-R GPS waveforms) for three different geometries from the range of viable strike-dip combinations shown in Fig. S1. Our results show that the geometry we adopted from previous InSAR studies (strike of  $259^{\circ}$  and dip of  $42.5^{\circ}$ ) explain the near-source seismic data the best. Nevertheless, the resulting finite-fault models do not change significantly in the range of possible strike-dip combinations (Fig. S2).

The fault is divided into 2.5 km by 2.5 km sized sub-faults. In the case of the 2011 Van earthquake, we used 38 sub-faults along strike and 16 sub-faults along dip, so the total fault length is 95 km and the depth range is between 2.5 and 29 km.

## 5 Velocity model and Green's functions

The kinematic Green's functions are generated by a frequency-wave number algorithm (Zhu and Rivera 2001). We attempted modeling the data using two different 1-D velocity structures. First of those two velocity models, a 1-D average of the velocity model developed by Zor et al. (2003) during the Eastern Turkey Seismic Experiment (ETSE) using receiver functions was found to be the one that fits the data the best. This velocity model is tabulated in Table 1. The second one is the Crust 2.0 velocity model at the hypocenter location (Bassin et al. 2000). We then compared the misfit to the two strong-motion and 1 H-R GPS waveforms. This comparison showed similar misfits, but overall the ETSE model fares slightly better; therefore, we prefer the ETSE model in our models (see the variance reduction of near-source data in Fig. 5 and Fig. S3, for the ETSE and Crust 2.0 models, respectively).

## 6 Results

### 6.1 Resolution tests

In order to analyze the sensitivity of each dataset with the given station geometry to the slip distribution, we performed synthetic tests for four different rupture scenarios and inverted for the slip distribution (Figs. 3 and 4).

In each scenario, we generated a slip distribution and picked a rupture velocity and rise time. In order to come up with more realistic estimates of the resolution, we added Gaussian white noise to the seismic and geodetic data using the signal-to-noise ratio (SNR) of the seismic data. We obtained the SNR by dividing the average of the power spectrum of the window that includes the data to a window that includes the background noise in the frequency range of the inversion (0.02 and 0.33 Hz). The SNR for the seismic data is listed in Table 2. The calculated SNR for the strong-motion data is very high ( $\sim 1 \times 10^5$ ). In order to consider unaccounted noise sources that scale with data, we assumed SNR of 500 for the strong-motion stations. For the H-R GPS data, we used half of the calculated SNR in Table 2 in order to account for the noise that scales with the data amplitude. For the teleseismic data we calculated, the average SNR for the P and the SH waveforms and added the seismic

**Table 1** The 1-D crustal velocity structure (ETSE Model) from Zor et al. (2003), used for the calculation of the Green’s functions

Thickness (km)	$V_p$ (km/s)	$V_s$ (km/s)	$\rho$ (g/cm <sup>3</sup> )	$Q_p$	$Q_s$
2.0	3.6	1.9	2.10	400	200
2.0	4.9	2.6	2.40	1,000	500
8.0	6.05	3.4	2.70	1,000	500
20.0	6.21	3.5	2.80	1,000	500
12.0	6.37	3.6	2.90	1,200	500

noise accordingly. We added random noise with the standard deviation of the reported GPS displacements.

In each scenario, we first performed a grid search to find the best-fitting rupture velocity using the joint

**Fig. 3** The results of the resolution tests 1 and 2. **a** The results of the grid search for finding the best-fitting rupture velocity. The variance reduction of the strong-motion and the all datasets are plotted against the rupture velocity. The red line shows the rupture velocity that is used for the input model. **b** The comparison of the input slip model and the inverted slip models using various datasets. The top plots show the input model that was used to generate the synthetic data. The datasets used in each model result is displayed on the left column. The hypocenter is represented by a red star. Rupture front contours are shown at every 2.5 s

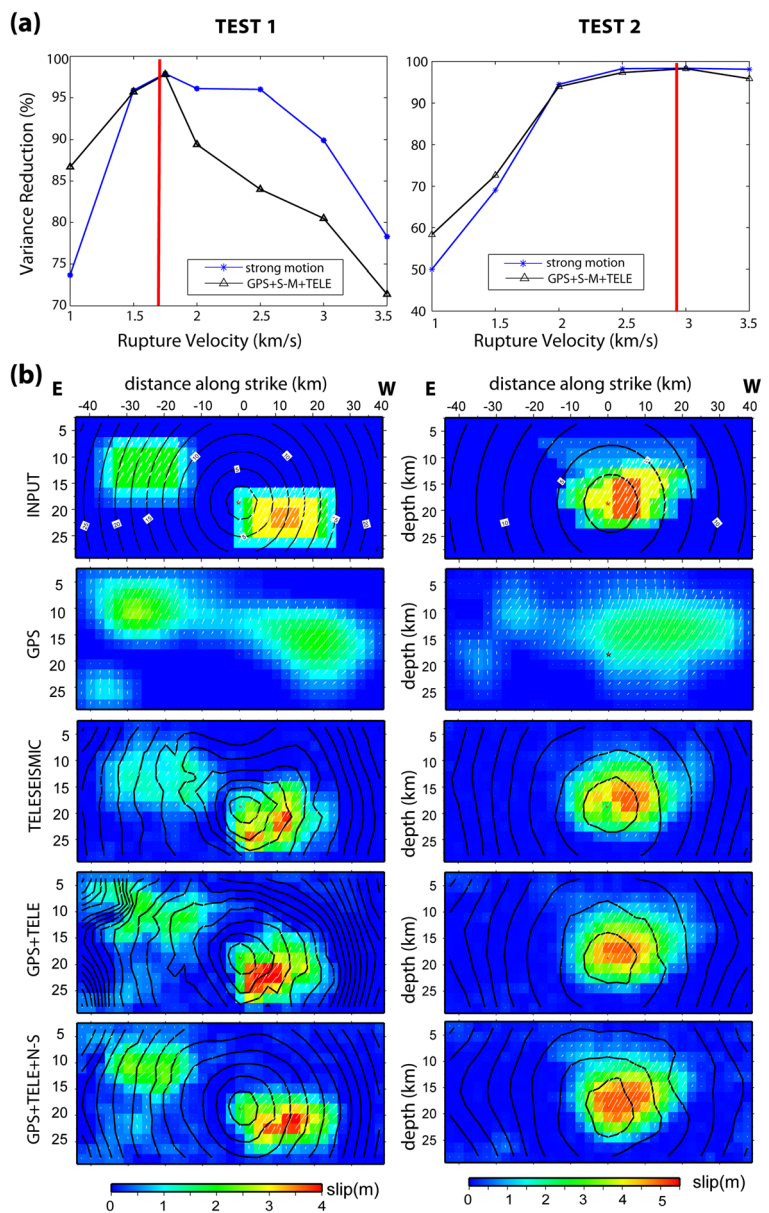


**Fig. 4** The results of the resolution tests 3 and 4. **a** The results of the grid search for finding the best-fitting rupture velocity. The variance reduction of the strong-motion and the all datasets are plotted against the rupture velocity. The red line shows the rupture velocity that is used for the input model. **b** The comparison of the input slip model and the inverted slip models using various datasets. The top plots show the input slip model used to generate the synthetic data. The datasets used in each model result is displayed on the left column. The hypocenter is represented by a red star. Rupture front contours are shown at every 2.5 s

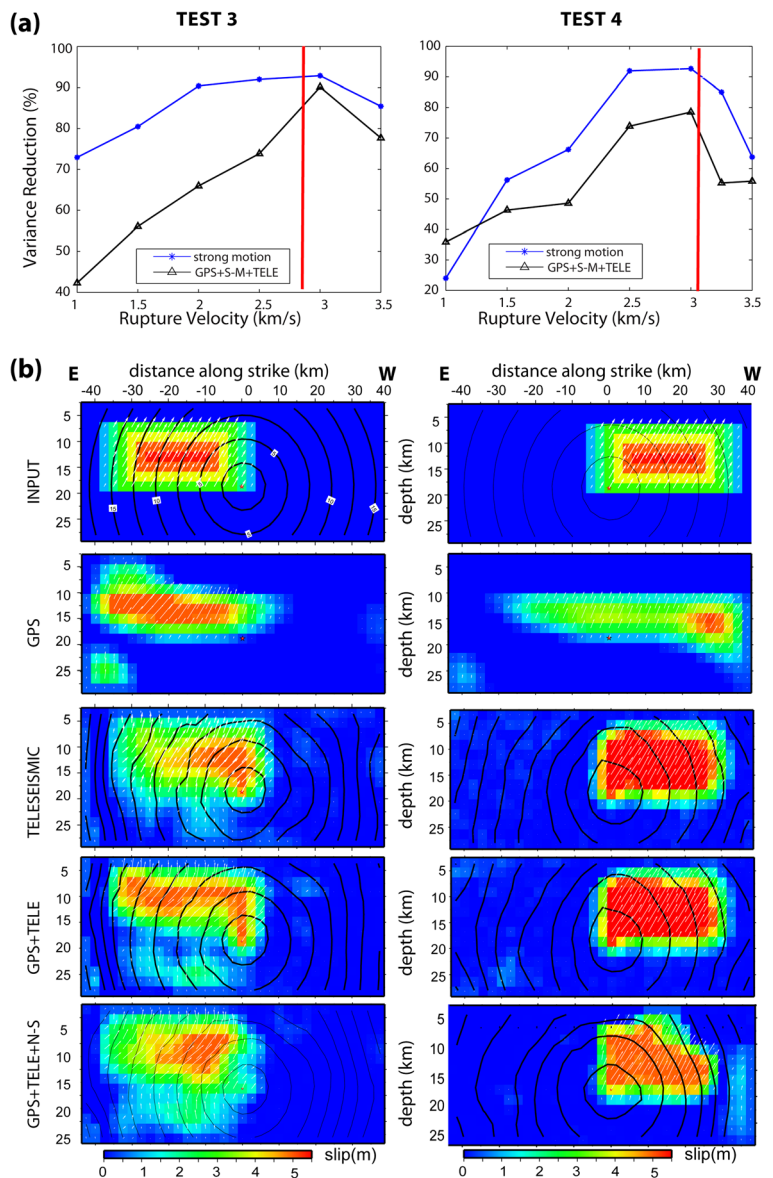


**Table 2** Signal-to-noise ratio (SNR) calculated from the power spectrum of the data and noise

Station Name	Type	Calculated SNR	Used SNR
MURA	H-R GPS East	81	40.5
MURA	H-R GPS North	125	62.5
BIT	S-M	$5.4 \times 10^5$	500
SIRT	S-M	$1.0 \times 10^6$	500
–	TELE. P	1250	500
–	TELE. SH	150	75

inversion of all the available synthetic datasets. We performed inversions using constant rupture velocities from 1 to 3.5 km/s. Then, we compared the misfit of each inversion to the given datasets. The comparison of the input rupture velocity to the best-fitting rupture velocity shows that although the near-source data are sparse, there is still some sensitivity to the rupture velocity (Figs. 3a and 4a). Once a reference rupture velocity was obtained from the grid search, we carried out the finite-fault modeling with variable rupture velocity with this reference rupture velocity (see Eq. 4).

Test 1 is designed to assess a bilateral rupture pattern where the asperity on the west of the hypocenter is deeper and accumulates more moment (Fig. 3). In Test 2, the slip is primarily toward west and up-dip and rupture expands bilaterally as it propagates up-dip (Fig. 3). This scenario is designed to mimic the Van earthquake slip distribution inferred from the initial modeling of the teleseismic data. Tests 3 and 4 are designed to test unilateral slip toward east and west, respectively (Fig. 4).

The results of the resolution tests show that the datasets included are sufficient to infer the details of the slip distribution. In each scenario, the slip distribution obtained from the inversion is reasonably similar to the input model. The distribution of the GPS stations is insufficient for resolving the slip distribution of this event. Overall, the joint inversions tend to be the ones that are most similar to the input model, showing the strength of combining various geodetic and seismic datasets. In addition when all datasets are included, the rupture time contours become more stable (Figs. 3 and 4).

Since we do not consider any biased errors or errors in Green's function, one can expect that the resolution for the actual slip distribution will be worse. In any case, in terms of geometry of the available data, the large-scale properties of slip are well-resolved with the available station distribution for the test cases considered here.

## 7 Constraining the average rupture velocity of the Van earthquake

Since our dataset is dominated by the seismic data, the resulting slip distribution depends on the rupture velocity used in the inversion. In our inversion scheme, rupture velocity can vary; however, the reference rupture velocity determined a priori in Eq. 4 still affects the overall properties of the rupture. Therefore, our first goal was to constrain the average rupture velocity, which was later used as a reference value for the variable rupture velocity inversions.

In order to determine the best-fitting rupture velocity, we performed a grid search of rupture velocity from 1 to 3.75 km/s and modeled the available near-source, teleseismic, and static GPS displacement data. We then tracked the VR of the near-source data and total VR (including all the

datasets) as we changed the rupture velocity (Fig. 5). We observe that both the near-source seismic data and total VR are sensitive to the rupture velocity. The rupture velocity and VR curves of Fig. 5 have double peaks, one around 2.0 km/s and a slightly higher peak between 3 and 3.5 km/s. The comparison of the strong-motion and high-rate GPS waveforms show that rupture velocity of 3.25 km/s is the best-fitting average value (Fig. 3).

In order to examine whether our results depend significantly on the velocity model used for the Green's functions, we perform the same analysis of finding the best-fitting constant rupture velocity using the velocity model from CRUST 2.0 (Bassin et al. 2000) at the hypocenter location (Table S1). The same analysis performed using the CRUST 2.0 model yields similar results with double peaks around 2 and 3.25 km/s (Fig. S2). The average rupture velocity obtained here and the double peaks observed for the VR is further examined in the "Discussion".

### 7.1 Slip distribution of the Van earthquake

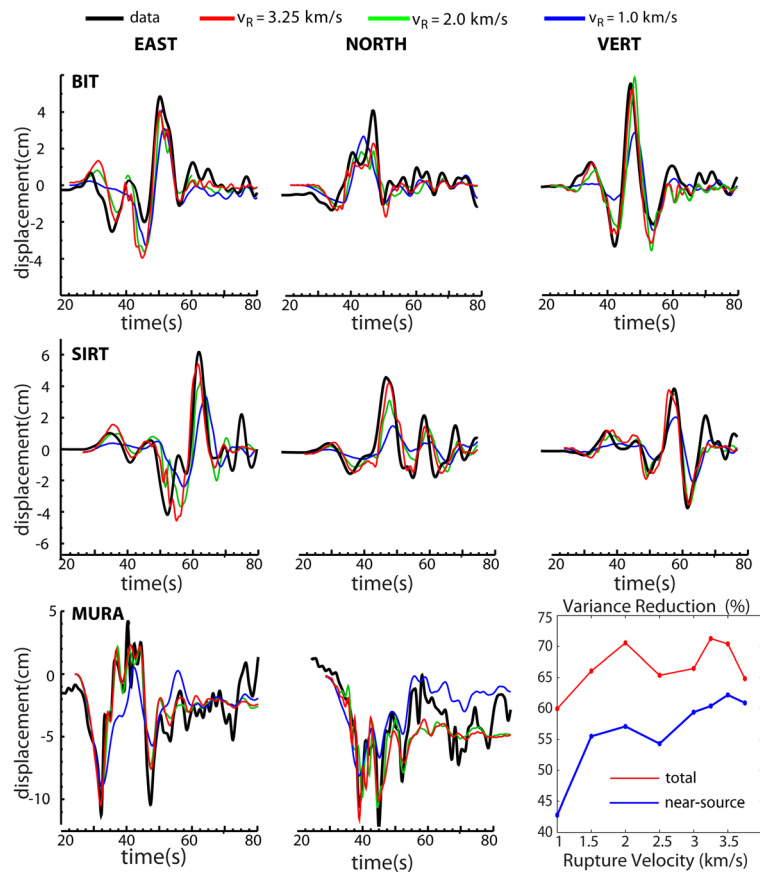
After obtaining the best-fitting rupture velocity, we performed inversions using variable rupture velocity for the earthquake using static GPS displacements, near-source, and teleseismic data and their various combinations (Fig. 6). Figure 6a shows the slip distribution obtained from the modeling of the GPS data. The GPS model shows that the largest slip is around the hypocenter. A shallow secondary slip patch is observed at 40–50 km west of the hypocenter and a very shallow slip patch is observed 20–30 km to the east of the hypocenter. Since the station distribution is sparse, the solution is highly sensitive to noise in data; therefore, these secondary shallow patches are likely to be artifacts.

The teleseismic slip model, shown in Fig. 6b, depicts a large slip patch around the hypocenter similar to the GPS model. There are other diffuse slip patches which are not easy to interpret, since it is not clear whether they are real or artifacts. The directivity of the largest slip patch around the hypocenter is up-dip and toward west.

The slip model using both teleseismic and GPS data is shown in Fig. 6c. This joint model resembles the teleseismic model except that the secondary slip patches move to greater depths.

When the strong-motion data is modeled along with the teleseismic and GPS data (Fig. 6c), directivity

**Fig. 5** The near-source data (black) and synthetics for various constant rupture velocity inversions using all the available data. The bottom right plot shows the variance reduction of the strong-motion data and all available data for the joint inversions using different rupture velocities



becomes clearer compared to the teleseismic and GPS models. The highest slip moves to the west of the hypocenter. In comparison to the GPS and teleseismic slip models, lateral rupture propagation toward east is more significant. Furthermore, the disconnected slip patches toward west, which are likely to be artifacts, are much smaller in size and amplitude in comparison to the GPS and teleseismic slip models.

Finally, we computed the model of all the available datasets by adding the waveform recorded at the H-R GPS station MURA, located at the northeast of the hypocenter (Fig. 1). In this model, there are clearly two slip patches, one larger asperity is up-dip and toward west of the hypocenter and a second smaller asperity is on the east of the hypocenter. The addition of the MURA station data provides a better constraint on the slip toward the east and the eastern slip patch becomes clearer.

We assume that the joint solution including all the data is the most viable solution since it explains the available datasets the best. In this slip

model (Fig. 6e), the main slip zone has a length of 45 km. The rupture starts propagating in the up-dip direction bilaterally with the highest slip of 4.5 m just to the west of the hypocenter. The slip is constrained between 8 and 20 km depth range. This implies that the shallower part of the Van fault has not ruptured in the 2011 earthquake. The asymmetry of the rupture time contours of Fig. 6e show that the rupture velocity toward east is slower than the one toward west.

The variance reductions to the associated datasets are tabulated in Table 3 for various models. The fits to the GPS data for the joint model of Fig. 6d are shown in Fig. 7, where most model estimates are in or close to  $1\text{-}\sigma$  error ellipses (Fig. 7) and variance reduction is 91 % (Table 3). In Fig. 7, the map view of the slip distribution for the model using all the data (Fig. 6e) is also shown. The largest asperity extends to the coastline of Lake Van to the west. The eastern slip patch is below Lake Ercek.

The fits to the near-source data for the joint model of Fig. 6e are shown in Fig. 8. The variance reduction for

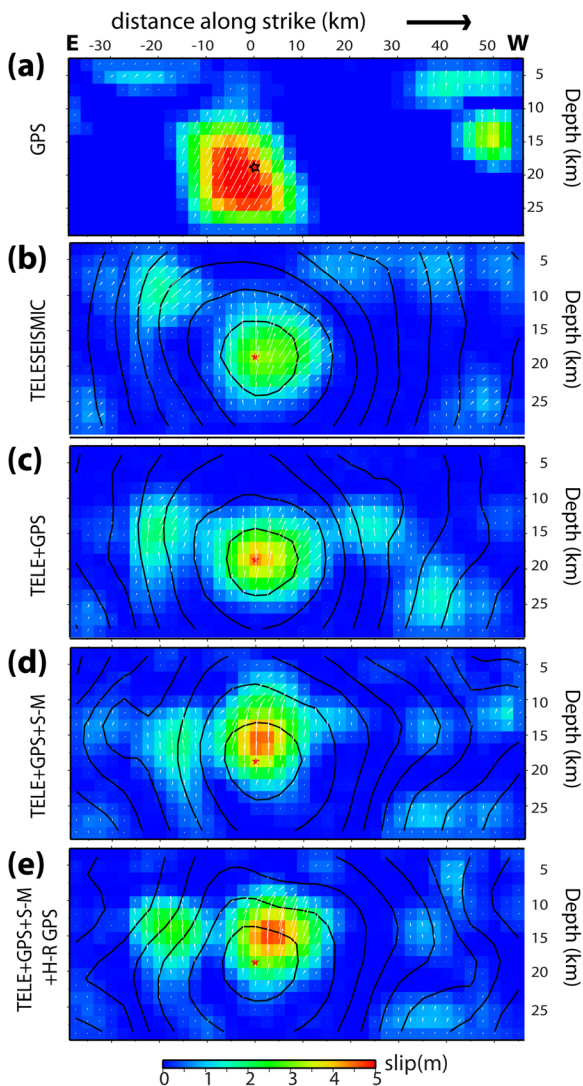


**Fig. 6** Slip distributions obtained using various combinations of the available datasets. The dataset used for each slip model is displayed on the left of the plots. The rupture front contours are shown every 2.5 s. The hypocenter is shown by the red star. *S-M* stands for the strong-motion data and *H-R GPS* stands for the high-rate GPS waveform data

this dataset for the joint model is 61.7 % (Table 3). The vertical components of the 1-Hz GPS are also shown although they were not part of the inversion.

The fits to the teleseismic data are also quite good (Fig. 8), but some discrepancies do exist between the SH waveform data and the synthetic waveforms. This might be because of the distortion of the SH waveforms when the source region has rough topography, which had also been observed for the 2005  $M_w$ 7.6 Kashmir Earthquake

(Avouac et al. 2006). The variance reduction for the joint model of Fig. 6e is 55.5 %, while when the teleseismic data is modeled by itself, the variance reduction is 80.1 % showing the discrepancies in teleseismic and other datasets (Table 3).

We use the same weight for the Laplacian smoothness parameter (20 % of the data error) for both the synthetic tests and the real data model. We verify the smoothness weight we use by calculating the *L* curve as shown in Fig. S4. The result shows that with the available data, the smoothness weight we choose is appropriate. The slip model can be smoothed slightly more than the chosen model here, but overall the kinematic model and its implications about the rupture extent and rupture velocity do not change while the peak slip values might change slightly depending on the weight of the smoothness constraint.

## 8 Discussion

### 8.1 Slip distribution of the 2011 $M_w$ 7.1 Van earthquake

A common feature of the slip models obtained from various combinations of datasets is that the largest slip patch is concentrated around the hypocenter. The size of this slip zone is roughly 40 km with a peak slip of 4.5 m to 5 m for all the slip models obtained from GPS, teleseismic, and near-source data.

An additional common characteristic of all the slip models is the lack of slip at the shallow part of the fault, as also noted in previous studies (Elliott et al. 2013; Fielding et al. 2013). The largest asperity is in the depth range of 8 to 20 km, without any significant shallow slip. This is a major concern, since the 2011 earthquake rupture has significantly loaded the shallower part of the fault. The post-seismic slip has taken place on the shallower portion of the Van fault and also on a shallow splay fault on the south of the main fault (Dogan et al. 2014). From the time of the earthquake to 1.5 years later, the total post-seismic slip on the shallower part of the fault is only 20 to 50 cm (Dogan et al. 2014). This is clearly not sufficient to accommodate the slip that occurred on the deeper part during the 2011 earthquake. Nevertheless, how the motion is accommodated at the shallower part of the Van fault is still an open

**Table 3** The variance reduction (VR) of each dataset for the models shown in Fig. 6

Dataset	GPS VR*	Tele. Waveform VR*	Near-Source Waveform VR*
GPS	94.6 %	–	–
TELESEISMIC	–	80.1 %	–
TELE+GPS	92.9 %	65.5 %	–
TELE+GPS+S-M	91.9 %	64.13 %	58.9 %
TELE+GPS+NS (S-M+HR GPS)	91.8 %	55.5 %	61.7 %

\*Variance reduction is calculated based on Eq. 1

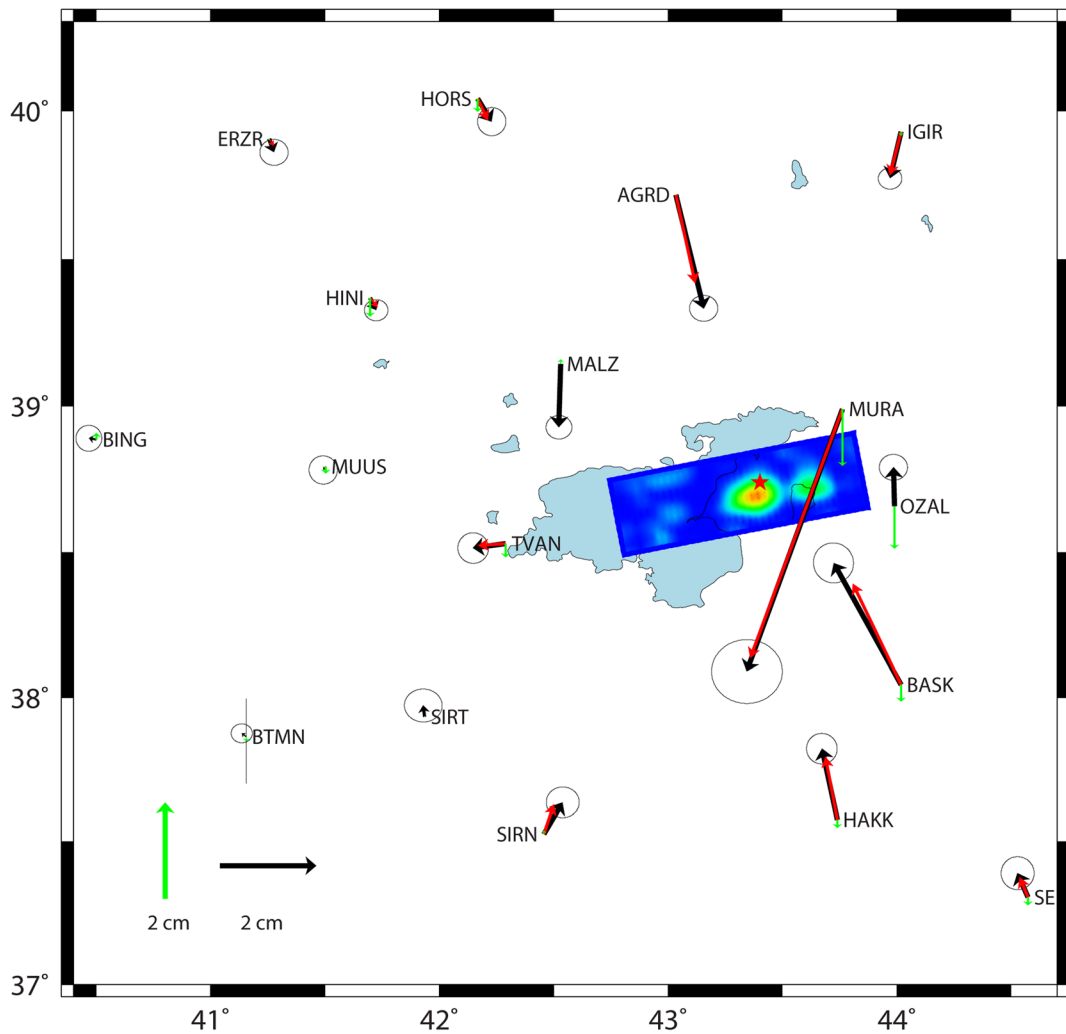
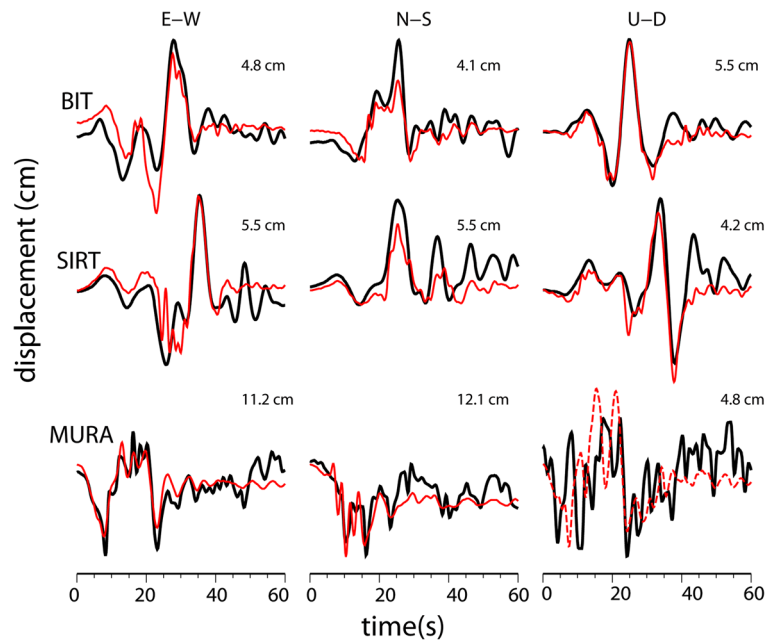


**Fig. 7** The map view of the solution using GPS, teleseismic, and near-source seismic data along with the fits to the GPS data. *Black arrows* are the static displacement measurements with 1- $\sigma$  error

*ellipses*, while the *red and green arrows* represent the horizontal and vertical model predictions, respectively

**Fig. 8** The fits to the three-component near-source displacement data, including two strong-motion and one high-rate GPS data. Data is in *black* and the synthetic waveforms are shown in *red*. The peak amplitude of each component is displayed at the *top right* of each waveform. The vertical component record of the H-R GPS stations MURA is also shown along with the synthetic prediction (*red dashed line*) although it was not included in the inversion



question and requires further monitoring, especially using geodesy.

One contribution of the near-source data is its sensitivity to rupture velocity and directivity. When the near-source seismic data are included (Fig. 6e), the two slip patches become clear; one up-dip and west of the hypocenter and a smaller slip patch at the east of the hypocenter.

We assume that the 2000  $M_w$ 5.3 earthquake at the western continuation of the 2011 rupture denoted in Fig. 1 ( $lat = 38.43$ ;  $lon = 42.96$ ), roughly marks the western end of the Van fault since events further west along the same strike direction suggest a strike-slip mechanism (Orgulu et al. 2003). Therefore, we infer that the Van fault terminates toward the western coast of Lake Van and about 35 km long segment of the fault beneath the lake possibly remains unbroken.

## 8.2 Comparison with other slip distribution models

So far, the slip distribution of the Van earthquake has been studied using InSAR and teleseismic data (Hayes 2011; Utkucu 2013; Fielding et al. 2013; Elliott et al. 2013). Here, we compare the slip distribution we obtained using joint inversion with the previous studies and discuss the possible reasons for the significant discrepancies among these models. Figure 10 shows our

final joint slip model and slip models from previous studies that were available to us. The slip distributions displayed in Fig. 10 show notable differences. Even if the same type of data is used, the slip distributions can differ significantly.

There are two published slip models that utilize the InSAR data, to this date (Fielding et al. 2013; Elliott et al. 2013). The InSAR models are critical for the 2011 Van earthquake since they provide the best coverage on the surface right above the rupture zone. The slip model generated by Fielding et al. (2013) using InSAR data shows a smooth slip distribution extending about 35–40 km along strike and between 5 and 20 km of depth with a peak slip of 3.5 m (Fig. 10b). Using the same InSAR tracks, Elliott et al. (2013) have come up with a solution which has two asperities with a tear of dip angle in between (Figure 10c). The peak slip is 10 m and the depth range is 10–20 km. The lateral extents of the two models are roughly the same; however, the differences between these two models in terms of slip distribution, segmentation, and roughness are remarkable.

To this date, there are two published slip models obtained from teleseismic data (Utkucu 2013; Fielding et al. 2013) in addition to the USGS NEIC finite-fault solution by Hayes (2011). The two solutions available to us were by Hayes (2011) and Utkucu (2013) (Fig. 10d–e). Utkucu (2013) found the rupture to be propagating unilaterally for 30 km toward west and up-dip with a

second patch at the eastern end. Slip distribution by Hayes (2011) shows a similar pattern of unilateral rupture although the largest slip patch is much closer to the hypocenter when compared to the model by Utkucu (2013). The teleseismic solution from Fielding et al. (2013), on the other hand, differs significantly where the peak slip is down-dip of the hypocenter while a second slip patch is up-dip and toward west. In the teleseismic model of Fielding et al. (2013), a disconnected secondary slip patch is located 20 to 40 km east of the hypocenter. To summarize, 2 out of the 3 teleseismic models considered here show primarily a unilateral rupture toward west although their slip patterns are quite different, while the third model shows the largest asperity in the down-dip of the hypocenter.

Gallovic et al. (2013) utilized the strong-motion data using a hybrid approach of finding multiple point sources and high frequency generation to obtain a slip model for the Van earthquake. The slip distribution obtained by Gallovic et al. (2013) is about 60 km and it is bilateral with longer propagation toward west. Since they utilize the near-source seismic data, the propagation toward east becomes evident in the slip model similar to our final model.

The joint kinematic solution of this study (Fig. 10a) is similar to the InSAR model by Elliott et al. (2013) in terms of segmentation. However, the asperities of the InSAR model are much more compact with unusually high slip values compared to our model and considering the size of the earthquake. In addition, the eastern asperity in our model is located about 10 km further east compared to the InSAR model by Elliott et al. (2013). Since in our solution, the reference rupture velocity that is determined from grid search is quite high (3.25 km/s), our model locates the eastern asperity further east. It is possible that the rupture velocity toward the west is close to 3 km/s while it is slower toward the east. The rupture does slow down toward the east compared to west in our model. However, since we penalize changes from the reference rupture velocity as given in Eq. 4, it is possible that the rupture velocity toward the east is even lower than what we obtain. A slower rupture velocity toward east would bring the eastern slip zone closer to the hypocenter than what we infer in our model. The kinematic properties of these two slip patches are further discussed in the next section.

The variations in the slip models obtained from different datasets (Fig. 10) show that the slip distribution of this event depends on the dataset and the inversion

method that are used to study the earthquake. This might reflect various issues, especially when only one type of data is used.

For example, in the teleseismic distances, all of the polarities of the P waves are the same due to primarily thrust mechanism of the 2011 earthquake (Fig. 9). The depth phases pP and sP destructively interfere with the initial positive pulse, creating uncertainty in pulse width and hence directivity, as well as the slip amplitude. For the ideal cases shown in the resolution tests, the slip distribution is still well-resolved since the minimum misfit is given by a slip distribution similar to the input model. However, when the slip distribution is more complex and there are possible biased errors due to Green's functions and other noise sources, slip models with different properties can explain the observed data with similar misfit values. Another factor that might contribute to the difference in the slip models is the difference in the methods used for modeling. For example, Utkucu (2013) has performed the inversion for velocity seismograms while Fielding et al. (2013) and Hayes (2011) have used displacement seismograms. Therefore the models obtained have different frequency sensitivities that might lead to the differences in the resulting slip models. The reported models may also differ in terms of the assumed rupture velocity, rise time function, and fault geometry, which then is mapped to the differences in slip distribution.

InSAR and GPS data, on the other hand, might suffer from the fact that the Van earthquake rupture does not extend to the shallow depths (<10 km), which increases the uncertainty due to the decreasing sensitivity of the geodetic data with depth (Simons et al. 2002; Page et al. 2009). Another problem with InSAR data might arise from the rough topography of the Van region, which leads to higher errors in the InSAR processing (Avouac et al. 2006). It is likely that one of the reasons for the difference in slip distribution of the two InSAR studies considered here (Fig. 10b, c) is the different amount of smoothing used in the inversion process.

This study shows that when various datasets are combined, the constraint on the slip distribution increases significantly and possible problems associated with one type of data can be overcome

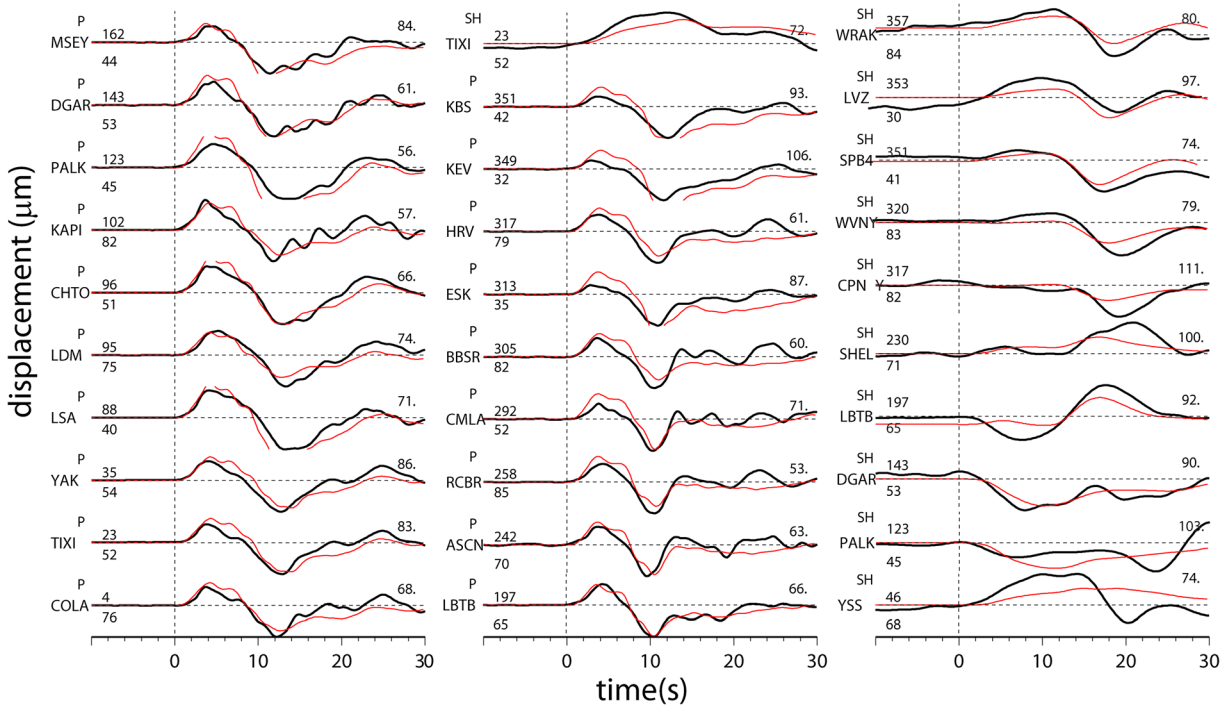


**Fig. 9** Telesismic P and SH waveform data (black) and synthetics (red). Station name, azimuth, and distance are indicated on the left of each trace. The maximum displacement is shown at the top right of each trace in microns

by adding another type of data with different sensitivity. In Table 3, we show the variance reduction associated with the datasets that are used in each inversion. It is important to note that when we compare the joint inversions with the single dataset inversion, the increase in the misfit for the GPS data is insignificant while the increase in the error for the teleseismic data is substantial (80 % VR for teleseismic model and 55 % VR for the joint model).

Hence, the 2011 Van earthquake represents a case where none of the datasets are sufficient to fully resolve the details of the slip distribution on their own. Therefore, rather than fitting one dataset perfectly, it is more important to fit multiple datasets in order to increase the resolution power for the slip. A similar conclusion was reached for the 1999  $M_w$ 7.4 Izmit earthquake by Delouis et al. (2002).

### 8.3 Rupture velocity and rise time of the 2011 Van earthquake

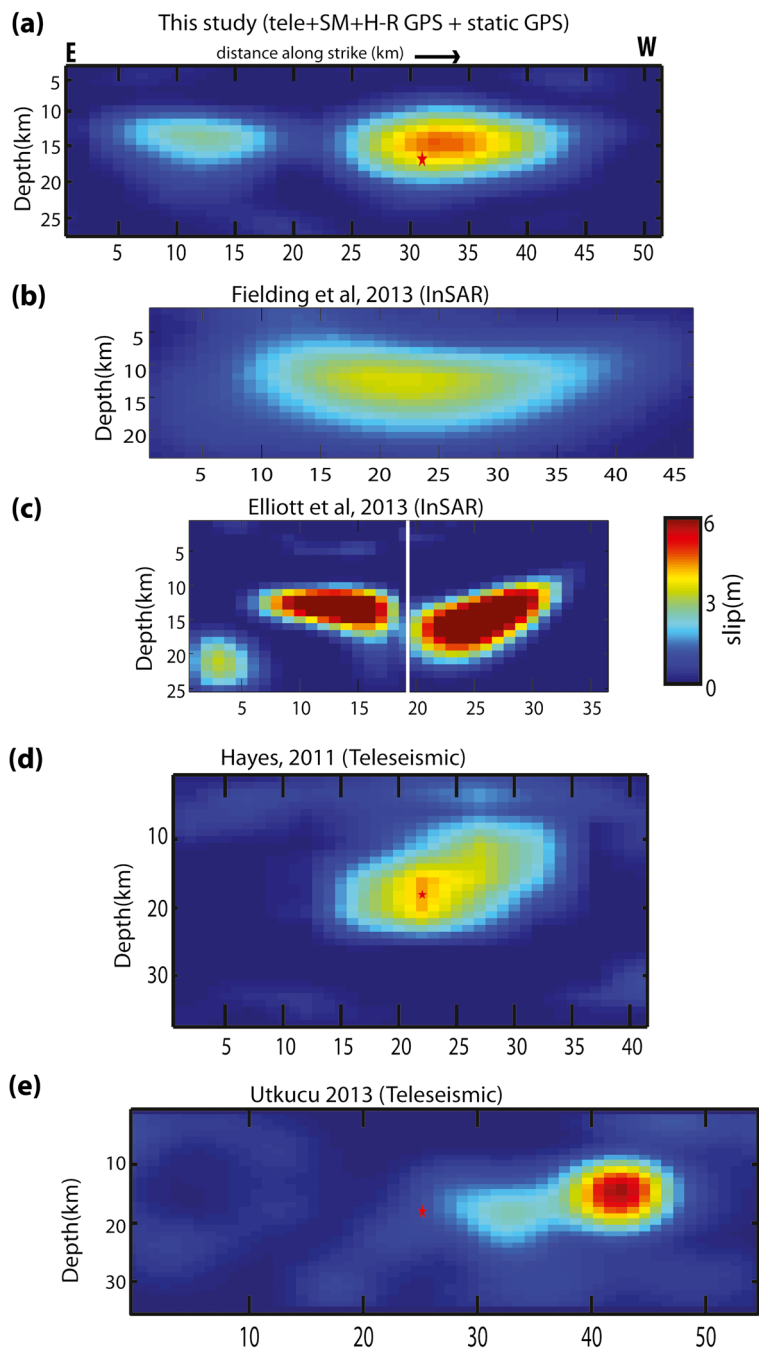
In the inversion process, we first determined the average reference rupture velocity as shown in Fig. 5. We then

performed a variable rupture velocity model using the reference rupture velocity of 3.25 km/s, where we allow the rupture velocity to vary between 2.4 and 3.6 km/s, and the rise time between 1 and 6 s. We used a single parameter slip-rate function with a predetermined cosine function shape and only inverted for the duration of the slip (rise time) in each sub-fault to avoid over-parameterization (Ji et al. 2002).

In order to determine the variations in rupture velocity, we calculated the slip-rate snapshots of the joint model (Fig. 11). In Fig. 8, the black contours show the rupture front contours for a rupture velocity of 3 km/s. The snapshots show that the rupture velocity is close to 3 km/s. This rupture velocity corresponds to 85 % of the shear wave velocity. The rupture snapshots show that the propagation toward the west is more dominant during the first 6 s, while between 6 and 10 s the eastern slip patch rupture is more significant. Overall, the rupture toward the east is delayed compared to the main asperity.

The delay of the eastern rupture can also be observed from the rise times. The rise time durations of the high slipping areas of this earthquake (Fig. 12) clearly show a significant difference between the eastern and the western slip patches.

**Fig. 10** Slip models from different studies of the 2011 Van earthquake. Slip models are aligned geographically. The *white line* in Fig. 10c marks a discontinuity in dip angle. The slip values are between 0 and 6 m. The slip model of Fig. 10c is saturated with peak slip of 10 m. All of the models are interpolated to 1 km by 1 km slip patches



The western patch has very short rise time duration with faster rupture velocity, while the rise time durations are much longer in the eastern patch. Figure S5 shows the histogram of rise times for sub-faults that slip more than 1.5 m for the eastern and the western slip patches, showing that

the peak rise time for the eastern slip patch is about 6 s while for the western segment it is 1–2 s.

This difference in rise time durations of the two segments might be a real phenomenon, but it might also be due to difference in the rupture

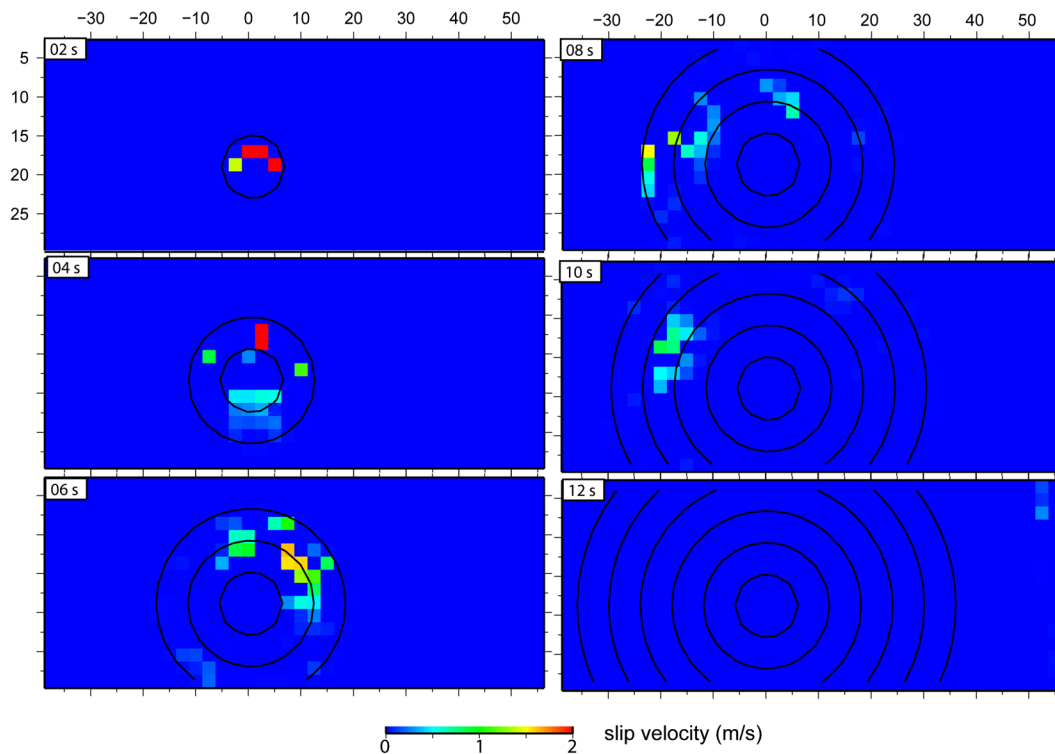


**Fig. 11** The snapshots of slip velocity at every 2 s. The *black contours* are the rupture front for a rupture velocity of 3 km/s and are shown for reference

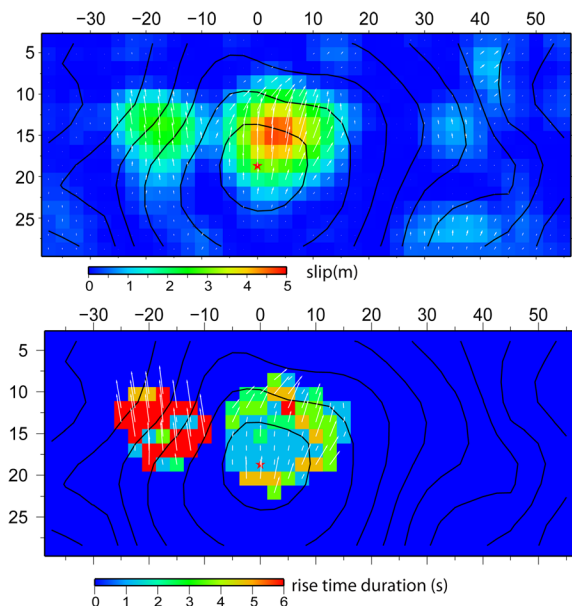


**Fig. 12** The slip distribution obtained from the joint inversion of all datasets (*top*), and the rise time duration of sub-faults with slip higher than 1 m (*bottom*) for the same kinematic model

velocities toward the east and the west or due to velocity model variations along the fault (Razafindrakoto and Mai 2014). When the near-source data is sparse, as is the case for this particular earthquake, there is a trade-off between rupture velocity and rise time. One interpretation is that the double peaks in the grid search for the best-fitting rupture velocity in Fig. 5 might correspond to the rupture velocities of the eastern and the western segments, respectively. A slower rupture velocity toward the east (~2 km/s or slower) and a faster rupture velocity toward the west (~3 km/s) might be a viable explanation for the grid-search results of Fig. 5. In this case, the eastern patch would be closer to the hypocenter, and our slip model might become more similar to the slip model from InSAR data by Elliott et al. (2013) and (Fielding et al. 2013) in terms of the extent of the rupture. Unfortunately, the current limits of finite-fault modeling and the sparsity of near-source data for this particular earthquake makes it impossible to differentiate between these two factors. Nevertheless, whether it is a

difference in rupture velocity or rise times or combination of these two effects, the behavior of the two slip patches are seismically different. Two separate sub-events with about 4 s delay in rupture time are also obtained by a multiple point source approach using the strong-motion data by Zahradnik and Sokos (2014). However, in their results, the second event is to the southwest, while in our model, the delayed secondary sub-event is toward the east of the hypocenter.

This difference in rupture velocity and/or rise time of the two slip patches might be due to a segmentation of the fault. Evidence for segmentation comes from the InSAR study of Elliott et al. (2013), in which, they observe offset of interferogram fringes and explain it using two fault segments with different dip angles with a tear in between the segments (Fig. 10c). In their best-fitting model, the western segment has a dip angle of 54° while the eastern segment has a dip angle of 40°.

## 9 Conclusion

The 2011 Van earthquake presents a challenging case because none of the available datasets is sufficient to resolve the slip distribution and the kinematic properties of the rupture on its own. Previous studies of this earthquake using various datasets reveal significant differences in terms of slip distribution. Even in the cases where the same datasets are used, the slip distributions can differ significantly. In this study, we modeled the 2011 Mw7.1 Van earthquake using static GPS displacements, teleseismic body waveforms, and near-source waveforms of strong-motion and 1-Hz GPS stations. Our results reveal that slip distribution is better-constrained when all the datasets are modeled simultaneously. Our joint kinematic model fits both the geodetic and the seismic data well. The rupture is bilateral with two slip patches; a larger patch which propagates up-dip and toward the west of the hypocenter reaching a peak slip of 4.5 m, and a smaller patch that propagates toward the east with a peak slip of 2.5 m. The slip is constrained between the depths of 8 and 20 km, revealing that the shallower part of the Van fault remained unbroken during the 2011 earthquake.

The average best-fitting rupture velocity is around 3 km/s; however, it is likely that the rupture velocity toward east is slower. The rise time of the western slip patch is about 1–2 s, while the eastern patch has much longer slip durations (~6 s). This difference in seismic behavior might be related to the segmentation of the fault as argued by a previous study of the 2011 earthquake using the InSAR data.

**Acknowledgments** This study was supported by Scientific and Technological Research Council of Turkey (TUBITAK) grant no: 112Y338. I would like to especially thank Prof. Semih Ergintav for the processing of the cGPS data. This manuscript has benefited greatly from the valuable comments of Dr. P. Martin Mai and one anonymous reviewer. I would like to thank Prof. Hayrullah Karabulut, Prof. Mustafa Aktar, and Dr. Yeliz Utku Konca for proofreading the manuscript.

## References

- Altiner Y, Sohne W, Guney C, Perl J, Wang R, Muzli M (2013) A geodetic study of the 23 October 2011 Van, turkey earthquake. *Tectonophysics* 588:118–134
- Arpat E, Saroglu F (1972) The East Anatolian fault system: troughs on its development. *Miner Res Explor Inst Turkey Bull* 78:33–39
- Avouac JP, Ayoub F, Leprince S, Konca O, Helmberger DV (2006) The 2005, Mw 7.6 Kashmir earthquake: sub-pixel correlation of ASTER images and seismic waveforms analysis. *Earth Planet Sci Lett* 249(3–4):514–528
- Barka A (1992) The North Anatolian fault zone. *Ann Tectonicae* 6:164–195
- Bassin C, Laske G, Masters G (2000) The current limits of resolution for surface wave tomography in North America. *Eos Trans* 81(48):S12A–03 (Fall Meet. Suppl.)
- Choi K, Bilich A, Larson K, Axelrad P (2004) Modified sidereal filtering: implications for high-rate GPS positioning. *Geoph Res Lett* 31(L22608) doi:10.1029/2004GL021621
- Delouis B, Giardini D, Lundgren P, Salichon J (2002) Joint inversion of InSAR, GPS, teleseismic, and strong-motion data for the spatial and temporal distribution of earthquake slip: application to the 1999 izmit mainshock. *Bull Seismol Soc Am* 92(1):278–299
- Delouis B, J-M N, Vallee M (2010) Slip distribution of the February 27, 2010 Mw=8.8 Maule Earthquake, central Chile, from static and high-rate GPS, InSAR, and broadband teleseismic data. *Geoph Res Lett.*, 37(17), doi: 10.1029/2010GL043899
- Dewey J, Hempton MR, Kidd WSF, Saroglu F, Sengor AMC (1986) Shortening of continental lithosphere: the neotectonics of Eastern Anatolia—a young collision zone. *Geol Soc Lond Spec Publ* 19(1):1–36
- Dogan U, Demir DO, Cakir Z, Ergintav S, Ozener H, Akoglu AM, Nalbant SS, Reilinger R (2014). Postseismic deformation following the  $M_w$  7.2, 23 October 2011 Van earthquake

- (Turkey): evidence for a seismic fault reactivation, *Geoph Res Lett.* 41, doi:10.1002/2014GL059291
- Dziewonski AM, Chou T-A, Woodhouse JH (1981) Determination of earthquake source parameters from waveform data for studies of global and regional seismicity. *J Geophys Res* B86:2825–2852
- Ekstrom G, Nettles M, Dziewonski AM (2012) The global CMT project 2004-2010: centroid-moment tensors for 13,017 earthquakes. *Phys Earth Planet Inter* 200-201, doi:10.1016/j.pepi.2012.1004.1002
- Elliott JR, Copley AC, Holley R, Schärer K, Parsons B (2013) The 2011 Mw 7.1 Van (Eastern Turkey) earthquake. *J Geophys Res*
- Emre O, Duman T, Ozalp S, Elmaci H (2011) Van depremi saha gözlemleri ve kaynak faya ilişkin Ön değerlendirmeler. Van earthquake Report, MTA
- Evangelidis CP, Kao H (2013) High-frequency source imaging of the 2011 October 23 Van (Eastern Turkey) earthquake by backprojection of strong motion waveforms. *Geophys Jour Int.* doi:10.1093/gji/ggt1437
- Fielding EJ, Lundgren PR, Taymaz T, Yolsal-Cevikbilen S, Owen SE (2013) Fault-slip source models for the 2011 M 7.1 Van earthquake in turkey from SAR interferometry, pixel offset tracking, GPS, and seismic waveform analysis. *Seismol Res Lett* 84(4):579–593
- Galovic F, Ameri G, Zahradnik J, Jansky J, Plicka V, Sokos E, Askan A, Pakzad M (2013) Fault process and broadband ground-motion simulations of the 23 October 2011 Van (eastern turkey) earthquake. *B Seismol Soc Am* 103(6):3164–3178
- Hayes GP (2011) Finite Fault Model Updated Result of the Oct 23, 2011 Mw 7.1 Eastern Turkey Earthquake, in [http://earthquake.usgs.gov/earthquakes/eqinthenews/2011/usb0006bqc/finite\\_fault.php](http://earthquake.usgs.gov/earthquakes/eqinthenews/2011/usb0006bqc/finite_fault.php), edited.
- Herring T (1998). Documentation for GLOBK: Global Kalman filter for VLBI and GPS analysis program, version 4.1. Mass Inst Technol, Cambridge
- Ji C, Wald D, Helmberger DV (2002) Source description of the 1999 Hector Mine, California earthquake, part I: wavelet domain inversion theory and resolution analysis. *Bull Seismol Soc Am* 92(4):1192–1207
- Ji C, Helmberger D, Wald DM, Ma KF (2003). Slip history and dynamic implications of the 1999 Chi-Chi, Taiwan, earthquake. *Journal of Geophysical Research-Solid Earth*, 108(B9), Art. No. 2412
- Ji C, Larson K, Hudnut K, Choi K (2004) Slip history of the 2003 San Simeon earthquake constrained by combining 1–Hz GPS, strong motion, and teleseismic data. *Geophys Res Lett* 31, L17608
- Konca AO, Hjørleifsdottir V, Song TRA, Avouac JP, Helmberger DV, Ji C, Sieh K, Briggs R, Meltzner A (2007) Rupture kinematics of the 2005 M-w 8.6 Nias-Simeulue earthquake from the joint inversion of seismic and geodetic data. *Bull Soc Am* 97(1):S307–S322
- Konca AO, Avouac JP, Sladen A, Meltzner AJ, Sieh K, Fang P, Li Z, Galetzka J, Genrich J, Chlieh M, Natawidjaja DH, Bock Y, Fielding EJ, Ji C, Helmberger D (2008) Partial rupture of a locked patch of the Sumatra megathrust during the 2007 earthquake sequence. *Nature* 456:631–635
- Konca AO, Kaneko Y, Lapusta N, Avouac JP (2013). Kinematic inversion of physically plausible earthquake source models obtained from dynamic rupture simulations. *Bull Seismol Soc Am* 103(5)
- Larson K, Bodin P, Gombert J (2003) Using 1-Hz GPS data to measure deformations caused by the Denali Fault earthquake. *Science* 300, doi: 10.1126/science.1084531
- Moro M, Canelli V, Chini M, Bignami C, Melini D, Stramondo S, Saroli M, Picchiani M, Kriakopoulos C, Brunori CA (2014) The October 23, 2011, Van (Turkey) earthquake and its relationship with neighbouring structures, *Sci. Rep.*, 4, doi: 10.1038/srep03959
- Orgulu G, Aktar M, Turkelli N, Sandvol E, Barazangi M (2003) Contribution to the seismotectonics of Eastern Turkey from moderate and small size events. *Geophys Res Lett* 30(24), doi:10.1029/2003GL018258
- Page MT, Custodio S, Archuleta RJ, Carlson JM (2009) Constraining Earthquake Source Inversions with GPS DATA 1: resolution based removal of artifacts. *J Geophys Res* 114(B01314). doi:10.1029/2007JB10005449
- Razafindrakoto HBT, Mai PM (2014) Uncertainty in earthquake source imaging due to variations in source time function and earth structure. *Bull Seismol Soc Am* 104(2), doi: 10.1785/0120130195
- Reilinger R, McClusky S, Vernant P, Lawrence S, Ergintav S, Cakmak R, Ozener H, Kadirov F, Guliev I, Stepanyan R, Nadariya M, Hahubia G, Mahmoud S, Sakr K, Arrajehi A, Paradissis D, Al-Aydrus A, Prilepin M, Guseva T, Evren E, Dmitrova A, Filikov SV, Gomez F, Al-Ghazzi R, Karam G (2006) GPS constraints on continental deformation in the Africa-Arabia-Eurasia continental collision zone and implications for the dynamics of plate interactions. *J Geophys Res* 111(B05411), doi:10.1029/2005JB004051
- Saroglu F, Emre O, Kuscu I (1992) Active fault map of Turkey. General Directorate of Mineral Research and Exploration, Ankara
- Sengor AMC, Yilmaz Y (1981) Tethyan evolution of Turkey: a plate tectonic approach. *Tectonophysics* 75:181–241
- Sengor AMC, Gorur N, Saroglu F (1985) Strike-slip faulting and related basin formation in zones of tectonic escape: Turkey as a case study, in *The Society of Economic Paleontologists and Mineralogists*, edited
- Simons M, Fialko Y, Rivera L (2002) Coseismic deformation from the 1999 M-w 7.1 Hector Mine, California, earthquake as inferred from InSAR and GPS observations. *Bull Seismol Soc Am* 92(4):1390–1402
- Utkucu (2013) 23 October 2011 Van, Eastern Anatolia, earthquake (MW 7.1) and seismotectonics of Lake Van area, *J Seismol*, 17, 783-805
- Wang GQ, Boore D, Tang G, Zhou X (2007) Comparisons of ground motions from collocated and closely spaced One-sample-per-second global positioning system and accelerometer recordings of the 2003 M 6.5 San Simeon, California, earthquake in the parkfield region. *Bull Seismol Soc Am* 97:76–90
- Wang R, Parolai S, Ge M, Jin M, Walter TR, Zschau J (2013) The 2011 Mw 9.0 Tohoku earthquake: comparison of GPS and strong-motion data. *Bull Seism Soc Am* 103(2B):1336-1347
- Yin H, Wdowinski S, Liu X, Gan WJ, Huang B, Xiao G, Liang S (2013) Strong ground motion recorded by

- high-rate GPS of the 2008  $M_s$  8.0 Wenchuan earthquake, China, *Seis Res Lett*
- Zahradnik J, Sokos E (2014) The  $M_w$  7.1 Van, Eastern Turkey, earthquake 2011: two-point source modelling by iterative deconvolution and non-negative least squares. *Geophys J Int* 196:522–538
- Zhu L, Rivera LA (2001) Computation of dynamic and static displacement from a point source in multi-layered media. *Geophys J Int* 148(3):1634–1641
- Zor E, Sandvol E, Gurbuz C, Turkelli N, Seber D, Barazangi M (2003) The crustal structure of the East Anatolian plateau (Turkey) from receiver functions. *Geophys Res Lett* 30(24) doi:[10.1029/2003GL018192](https://doi.org/10.1029/2003GL018192)